Journal of
Materials Chemistry B

ROYAL SOCIETY
OF CHEMISTRY

PAPER

View Article Online
View Journal

Check for updates

Cite this: DOI: 10.1039/d5tb02844b

Conjugating M13 bacteriophage targeting folate receptor alpha with multiple photosensitizers: a flexible phototheranostic platform against ovarian cancer

Alena Kaltenbrunner, †[ad] Andrea Martino, †[b] Michela Nigro,†[ad]
Andrea Carboni, [bd] Alessia Marconi, [bd] Nicolò Mercorelli, [b]
Manuele Di Sante, [bd] Chiara Di Donato, [b] Annapaola Petrosino, [a]
Simona Corrà,[c] Monica De Luise,[c] Giuseppe Gasparre, [c] Matteo Calvaresi, [bd]
Alberto Danielli,[ad] Paolo Emidio Costantini *[ad] and Matteo Di Giosia *[bd]

Ovarian cancer remains one of the deadliest malignancies in women, largely due to late-stage diagnosis and limited efficacy of current chemotherapies. To address this challenge, we introduce an advanced phage-based phototheranostic platform that leverages genetic programmability and modular chemical functionalization for selective tumor eradication. We first generated a single-chain variable fragment derived from the anti-folate receptor α (FRα) antibody MORAb-003, then we engineered M13 bacteriophage displaying this targeting moiety, enabling high-affinity recognition of FRα-overexpressing ovarian cancer cells. Using orthogonal bioconjugation, we then conjugated multiple copies of two complementary photosensitizers, chlorin e6 (Ce6) and rose bengal (RB), onto the phage capsid, yielding a photoresponsive nanoconstruct with dual excitation/emission profiles. This multifunctional viral scaffold seamlessly integrates tumor targeting, fluorescence imaging, and light-activated cytotoxicity into a single biocompatible architecture. The resulting $\mathrm{M13_{FR\alpha}}$–Ce6–RB conjugates exhibit potent photodynamic activity under both red and green light irradiation, highlighting the potential of refactored M13 phages as flexible nanocarriers for precision phototherapy. This work presents a customizable and translationally relevant nanoplatform for image-guided treatment of chemoresistant ovarian cancer and other FRα-positive malignancies.

Received 18th December 2025,
Accepted 21st April 2026

DOI: 10.1039/d5tb02844b

rsc.li/materials-b

Introduction

Ovarian cancer (OC) is the fifth leading cause of cancer death in women. Despite its lower incidence compared to other female cancers, it is a particularly lethal malignancy. In 2020, over 300 000 new cases of ovarian cancer were estimated worldwide. Due to the relatively asymptomatic nature of OC and advanced disease present at the time of diagnosis, the survival rate five years after recognition is around 40%, causing the death of over 200 000 women every year.[1] The high case fatality rate underscores the urgent need for continued research into its etiology, early detection methods, and more effective treatment strategies. Among the main causes contributing to this scenario is the lack of effective biomarkers for detecting early-stage illness, predicting clinical response, and determining clinical regimes.[2–4]

Currently, the standard procedure for treatment of advanced OC is based on a combination of debulking surgery and paclitaxel and platinum-based chemotherapy. However, disease recurrence occurs in most patients due to platinum chemotherapy resistance and the high degree of heterogeneity of the tumor microenvironment.[5,6]

Innovative oncology strategies often rely on combining different therapeutic modalities to offer potential improvements over a single therapy, aiming to address chemoresistance. Moreover, fluorescence-guided surgery has emerged as a

---

[a] Department of Pharmacy and Biotechnology, Alma Mater Studiorum – University of Bologna, via Francesco Selmi 3, Bologna 40126, Italy
[b] Department of Chemistry "Giacomo Ciamician", Alma Mater Studiorum – University of Bologna, via Piero Gobetti 85, Bologna 40129, Italy. E-mail: matteo.digiosia2@unibo.it
[c] Department of Medical and Surgical Sciences (DIMEC), Medical Genetics and Centro Studi e Ricerca sulle Neoplasie Ginecologiche University of Bologna, Bologna, Italy
[d] Istituto di Ricerca e Cura a Carattere Scientifico (IRCCS) AOUBO Sant'Orsola – Laboratory of Preclinical and Translational Research in Oncology (PRO), Bologna 40138, Italy

† These authors contributed equally to this work.

new technique that guides surgeons in the selective resection of OC, and image-guided photodynamic therapy (PDT) could represent a promising tool, further improving the treatment selectivity.[7,8]

Photodynamic therapy is a minimally invasive therapeutic modality that has been clinically approved for the treatment of several conditions, including certain cancers and dermatological disorders.[9–11] The therapeutic effect of PDT relies on the interplay of three essential components: (i) a light source in the visible or near-infrared range; (ii) a photosensitizer (PS), *i.e.*, a compound capable of absorbing light energy and displaying peculiar photophysical properties; and (iii) molecular oxygen physiologically present in the target cellular tissue. Following systemic or local administration, an ideal PS preferentially accumulates within cancer cells. Upon irradiation with light of an appropriate wavelength, the PS is activated, sensitizing molecular oxygen and generating reactive oxygen species (ROS). The high local concentration of ROS induces oxidative stress, leading to cytotoxicity in neoplastic cells. PDT-mediated tumor eradication *in vivo* involves three distinct mechanisms, or their synergistic action: (i) the activation of programmed cell death (*i.e.*, apoptosis, ferroptosis); (ii) the direct damage to cancer-associated vasculature, leading to tumor infarction; (iii) the activation of an acute inflammation and induction of the host defense immune response, which can subsequently attack cancer cells.[12]

Since OC is most often confined within the peritoneal cavity, the disease is amenable to regionally localized PDT.[13–16] In this setting, light delivery does not rely on transcutaneous penetration but can instead be achieved through fiber-optic illumination directly within the peritoneal cavity during image-guided procedures. This is particularly relevant for ovarian cancer, which often presents as superficial peritoneal implants and residual nodules after cytoreductive surgery, making direct illumination clinically feasible. PDT is suitable as a complementary treatment to chemotherapy to reduce residual tumor volume. Within this framework, red-light activation provides greater tissue penetration, while green-light activation can complement treatment of superficial lesions under direct intracavitary illumination. Reducing the overall tumor burden improves the ability of chemotherapeutics to penetrate tumor cells and enhances treatment efficacy by reducing the number of chemotherapy cycles, thus preventing the onset of chemoresistance.

Several classes of molecules are commonly used as PS, *e.g.*, porphyrinoids, xanthenes, fullerenes, and oligothiophenes, which exhibit high photophysical performance as both photodynamic and imaging agents.[17–19] Although they have demonstrated very high performances as a free molecule (*i.e.*, second-generation PSs), they still present important limitations in their translation into clinics, due to their (i) hydrophobicity and tendency to aggregate, (ii) poor biocompatibility and stability under physiological conditions, (iii) low cancer-to-normal cell preferential accumulation, and (iv) poor pharmacokinetic and pharmacodynamic profile.

Although the selectivity of PDT is spatially governed by the localized irradiation, a suitable targeting vehicle capable of selectively delivering PSs (*i.e.*, third-generation PS) into the OC cell is still missing. To design a suitable carrier addressing the PSs toward OC cells, the first step is the identification of a biomolecular target maximizing the cancer-to-normal cell ratio. Folate receptor α (FRα), a 38–40 kDa glycosyl-phosphatidylinositol (GPI)-anchored cell-surface glycoprotein, was found to be constitutively expressed in up to 90% of OCs, overexpressed in 70% of primary OCs, and 80% of recurrent OCs express FR. In contrast, non-malignant ovarian tissue does not express or barely expresses folate receptor, making it an appealing oncotarget for the selective delivery of anticancer agents.[20–22] The first evidence that FRα is a druggable target was farletuzumab (MORAb-003), a humanized monoclonal antibody antagonizing FRα.[23,24] However, the phase III trial demonstrated that the addition of farletuzumab to standard chemotherapy did not significantly improve the progression-free survival (PFS) in platinum-sensitive recurrent OC.[25] Mirvetuximab soravtansine (Elahere) is an antibody–drug conjugate (ADC) specifically designed to target FRα. It combines a monoclonal antibody directed against FRα with DM4, a cytotoxic maytansinoid that disrupts microtubule function, enabling targeted delivery of chemotherapy to cancer cells. Approved by the FDA in 2022, Elahere is indicated for the treatment of platinum-resistant epithelial ovarian cancer with high FRα expression, particularly in patients who have received one to three prior lines of systemic therapy.[26] To address the main restraint of ADCs, related to the limited amount of payload conjugated to the antibody, in recent years, our research group has demonstrated the opportunity to use M13 bacteriophages (phages) as a multifunctional biotechnological platform.

Bacteriophages are ubiquitous viruses that infect bacteria but are inactive against eukaryotic cells.[27,28] Phages are highly

Matteo Di Giosia

Matteo Di Giosia is a Junior Assistant Professor of Organic Chemistry at the University of Bologna and a researcher at the IRCCS Sant'Orsola Hospital (Bologna, Italy). His research focuses on the design of biohybrid and protein-based materials for nanomedicine, with particular emphasis on bioconjugation chemistry, bacteriophage engineering, and photoactive nanomaterials for imaging and photodynamic therapy. He received his PhD in Chemistry from the University of Bologna and carried out research periods as a visiting fellow at University College Dublin and at the Technion – Israel Institute of Technology. He has been Principal Investigator of several competitive research projects, and his work bridges materials chemistry and translational biomedical applications, aiming to develop modular and programmable platforms for precision theranostics.

uniform in size and morphology, stable over a wide range of pH and temperature, and in the presence of nucleases and proteases. The M13 filamentous phage has received increasing attention as a well-defined protein-based platform for the assembly of nanostructured functional molecules and materials.[29] M13 exhibits a tube-shaped virion with a very high aspect ratio (∼900 to 7 nm), composed of a single-stranded DNA encapsulated within major coat proteins (pVIII), counting about 2700 copies and constituting the capsid side wall. Minor coat proteins (*i.e.*, pIII, pVI, pVII, pIX), of about 5 copies each, cap the two extremities. Given the genetically tunable surface chemistry and its potential to self-assemble into hierarchical structures, M13 was recently rediscovered as a suitable biotechnological platform for the nanometric ordered assembly of functional molecules. Although M13 does not infect or replicate in mammalian cells, its potential immunogenicity remains an important consideration for translational development. More generally, clinical experience with bacteriophage administration suggests that phage-induced immune responses are measurable but typically manageable, rather than representing a prohibitive barrier.[30–32] Thus, immunogenicity should be regarded as a relevant variable in the development of phage-based nanoplatforms.

Phage display is a molecular technique based on the genetic modification of phage DNA to enable the expression of peptides/proteins on the phage surface, in fusion with one of the wild-type (WT) phage coat proteins. The pIII protein tolerates extensive modifications and, therefore, can be efficiently used to display large peptides or protein copies on phage (*e.g.*, scFv, Fab, nanobodies, affibodies) without markedly affecting pIII stability. Compared with other delivery platforms explored in ovarian cancer, particularly liposomal and polymeric nanocarriers, M13 phage offers the distinctive advantage of combining selective genetic targeting and high-density chemical functionalization within a single, structurally defined scaffold. This feature is particularly attractive for third-generation photosensitizer delivery, where both receptor recognition and high payload density are required. In principle, M13 can be retargeted to cancer cell receptors through the display of specific sequences on pIII. At the same time, therapeutic and imaging molecules can be conjugated in multiple copies onto pVIII, making this phage an attractive scaffold for phototheranostic applications.[33] In M13, such therapeutic and/or imaging agents can be bioconjugated in hundreds of copies onto pVIII, providing a robust and flexible platform for anticancer approaches.[34]

Following such an orthogonal approach, our research group has successfully demonstrated the possibility of using refactored M13 as a versatile platform for the selective treatment of cancers overexpressing specific antigens, suitable as an anticancer target (epidermal growth factor receptors, disialoganglioside-GD2, fibronectin receptor).[35–39]

In this work, we developed a third-generation photosensitizer-conjugated phage nanocarrier by introducing a newly designed targeting module. We first engineered a single-chain variable fragment (scFv) derived from the anti-folate receptor α (FRα) antibody MORAb-003, generating a novel ligand with high specificity for FRα. This scFv was then genetically fused to the M13 pIII protein, enabling its selective display on the phage tip and conferring targeted recognition of FRα-overexpressing ovarian cancer cells.

Results and discussion

Redesign the M13 phage to target the FRα of OC cells

A phage-based platform was designed to selectively address photosensitizers toward ovarian cancer cells overexpressing the folate receptor α. M13 with targeted tropism ($M13_{FR\alpha}$) was developed by displaying in multivalency on the phage tip a scFv derived from MORAb-003. The scFv sequence (see SI) was generated by linking the VH and VL domains of MORAb-003 with a flexible peptide linker (3× GGGGS), and codon-optimizing the construct for *E. coli* expression. In principle, this design preserves the structural determinants required for high-affinity FRα recognition. The scFv coding sequence was cloned in frame with the C-terminal domain of the minor coat protein pIII under the control of the inducible pRham promoter (pPK3003-MORAb phagemid). Engineered phage, $M13_{FR\alpha}$, was produced by co-transforming *E. coli* DH5α with the phagemid and the M13KO7Δg3pΔoriF1 hyperphage plasmid, which encodes all M13 proteins except pIII (Δg3p) (Fig. 1A). The use of viral replication origin-deleted hyperphage (ΔoriF1) enables the exclusive packaging of the pPK3003A_MORAb phagemid inside the virion, resulting in homogeneous phage length.[40] The presence of scFv anti-FRα fused to the C-terminal domain of the minor coat protein pIII was confirmed by intact protein analysis using liquid chromatography (LC) coupled to mass spectrometry (MS). A procedure was optimized, based on previous methodologies[41,42] (see Materials and methods) to isolate the $M13_{FR\alpha}$ capsid proteins, leading to the identification of the modified pIII at the expected molecular weight of 46.4 kDa (Fig. 1B). The expression of the pIII–scFv fusion protein was further confirmed by western blot analysis using an anti-pIII antibody (Fig. S1). It is worth noting that powerful MS analysis has seldom been employed for the characterization of phage coat proteins, particularly for the identification of the less abundant pIII. For instance, Hess *et al.*[43] characterized pIII fusion products after gel electrophoresis separation, gel extraction, and tandem MS analysis of the corresponding peptides. Here, for the first time, we employed LC separation to allow the straightforward identification of the intact protein by native ESI-MS.

A selection of five different OC cell lines (OV90, OVSAHO, CAOV3, SKOV3, OC314) was used as a panel to assess the retargeting performance of $M13_{FR\alpha}$. These cell lines were selected to represent a biologically heterogeneous *in vitro* panel, including differences in anatomical origin and genetic background (Table S1), and spanning a broad range of FRα expression levels. This panel therefore enabled evaluation of the relationship between receptor abundance and phage targeting efficiency. The validation of cell lines (Table S1) and the estimation of the FRα expression were preliminarily carried

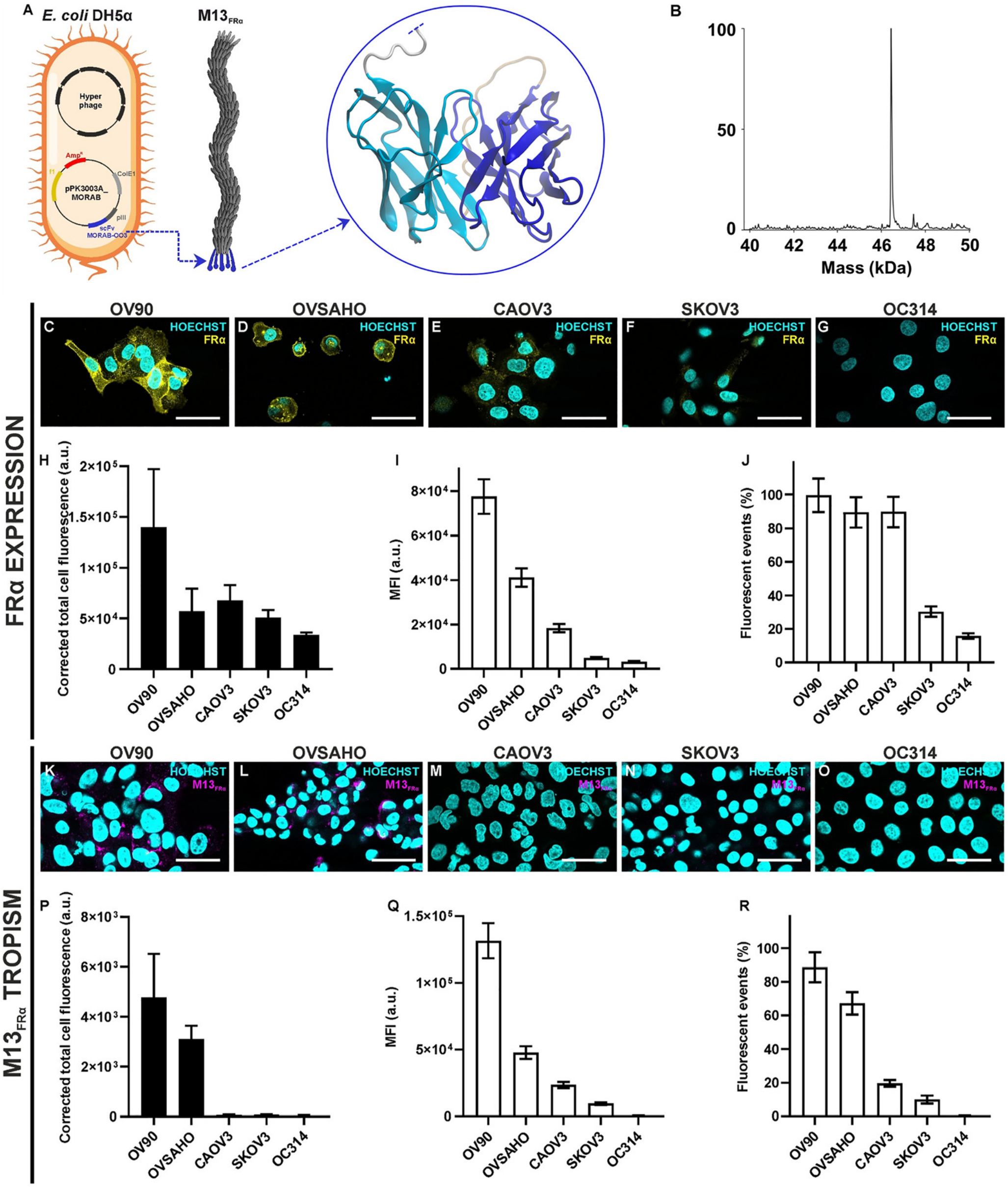

Fig. 1 FRα expression levels and targeting of the $M13_{FR\alpha}$ towards OC cells. (A) Phage modification scheme, the scFv MORAb-003 coding sequence was cloned in frame with pIII (grey), generating the pK3003A-MORAb phagemid. Co-transformed bacteria produced the modified phages. Inset: 3D structure of scFV derived from MORAb-003 expressed in fusion with the pIII (truncated). (B) Deconvolved MS spectra of pIII protein. Immunocytochemical confocal microscopy of OV90 (C) and (K), OVSAHO (D) and (L), CAOV3 (E) and (M), SKOV3 (F) and (N) and OC314 (G) and (O) were incubated with the anti-FRα mAb antibody ((C)–(G) in yellow) or with $M13_{FR\alpha}$ ((K)–(O) in magenta), nuclei are in cyan. White lines in the confocal images represent the scale bars (50 μm). Semi-quantitative fluorescence confocal microscopy analysis (H) and flow cytometry analysis of the FRα expression (I) and (J). Semi-quantitative fluorescence confocal microscopy analysis (P) and flow cytometry analysis (Q) and (R) of the retargeting ability of $M13_{FR\alpha}$ on all the cell lines. (I) and (Q) Mean fluorescence intensity (MFI) of all the cell lines incubated with anti-FRα or $M13_{FR\alpha}$. (J) and (R) Percentage of fluorescent events calculated in flow cytometry. All graphs and calculations performed using Graphpad Prism and FlowJo™.

out to ensure the robustness of the *in vitro* characterizations. Immunocytochemical confocal microscopy (Fig. 1C–H) and cytofluorimetry (Fig. 1I and J), performed using a commercial anti-FRα mAb (clone 548908), revealed different levels of FRα expression, in agreement with the literature data: OV90 > OVSAHO > CAOV3 > SKOV3 > OC314.[44–46] Representative fluorescence intensity histograms are reported in Fig. S2 to illustrate the homogeneous FRα expression across the cell panel. The specific tropism of $M13_{FR\alpha}$ was then investigated and validated using the same techniques. OC cell lines were incubated with 1×10^{12} $M13_{FR\alpha}$, and a FITC-labelled anti-pVIII mAb was used for the estimation of $M13_{FR\alpha}$ tropism towards OC cell lines. $M13_{FR\alpha}$ binding level to OC cell lines correlates with folate receptor expression grade. Indeed, confocal microscopy images (Fig. 1K–O) supported by semi-quantitative analysis (Fig. 1P) and flow cytometry data (Fig. 1Q and R) confirmed the major avidity of $M13_{FR\alpha}$ for OV90 and the reduced affinity for OC314, which has low FRα expression. Also in the other OC cell lines, $M13_{FR\alpha}$ showed a preference for OVSAHO, CAOV3 and SKOV3 cells in decreasing order of affinity, which is consistent with their relative FRα expression levels. To further validate the specificity of $M13_{FR\alpha}$, a competition assay was performed by pre-incubating OV90 cells with the anti-FRα monoclonal antibody prior to phage incubation. A significant reduction in phage binding was observed, further supporting FRα-specific targeting (Fig. S3). Taken together, these data proved that M13, engineered to express an anti-FRα scFv on the pIII minor coat protein (up to five copies per phage) retains receptor-binding capability comparable to that of a commercial mAb. Such a highly selective behavior is not new for engineered phages displaying targeting moieties on the phage tip, and it has previously been demonstrated for multiple cellular receptors.[35,37,38] Nevertheless, this study reports the first retargeting of M13 phage toward FRα using an antibody-derived scFv – a ligand that we have *de novo* engineered for this purpose. In contrast, previous attempts to redirect M13 phages to the folate receptor relied exclusively on peptides or oligopeptides.[47,48]

Based on this screening, we selected the cell lines belonging to the two ends of the panel for subsequent experiments: OV90, expressing the highest levels of FRα, and OC314, which expressed the lowest FRα levels. While the selection of OV90 is obvious, the evaluation of the treatment on cell lines displaying a low expression of FRα, such as OC314, results in an attractive approach to address the limitation of current targeted therapies for OC.

Orthogonal bioconjugation of $M13_{FR\alpha}$ with Ce6 and RB photosensitizers

The use of the M13 phage-based platform offers the opportunity of conjugating hundreds of therapeutic and/or imaging molecules to its capsid proteins. It follows that different classes of photosensitizers, displaying complementary photophysical properties, can be conjugated to a single M13 phage. In contrast with previous studies focusing on conjugation of a single chemical species, herein we combined a xanthene- and a chlorin-based photosensitizer, Rose Bengal (RB) and chlorin e6 (Ce6), respectively, as already used photosensitizers for PDT treatment. Ce6 and RB were selected as complementary photosensitizers to extend light absorption over a broader region of the visible spectrum. To the best of our knowledge, this work represents one of the first examples of an engineered M13 bacteriophage covalently functionalized on pVIII with two distinct photosensitizers for targeted PDT applications.

A chemoselective bioconjugation of RB was performed using a two-step conjugation procedure:[28] (i) the transamination reaction on the N-terminal Ala1 of the pVIII and (ii) the coupling of N-terminal ketones with the RB-alkoxyamine derivative (RB-PEG$_3$-ONH$_2$), previously synthesized from RB. As a second step, carbodiimide-mediated coupling was used for Ce6 bioconjugation, activating a carboxyl group with EDC/NHS, and targeting the available primary amines of the pVIII, *i.e.*, Ala1 and Lys8 (Fig. 2A). This sequence was chosen because performing Ce6 conjugation first would likely reduce the number of sites available for subsequent RB coupling, further biasing the final Ce6/RB loading ratio.

After conjugation and purification, the absorption spectra of the bioconjugates confirmed the effective linkage of both PSs (Fig. 2B). The main absorption bands of Ce6 are observed around 400 and 650 nm (Fig. S4A), while the characteristic band of RB can be identified at a higher wavelength, in the 400–600 nm range (Fig. S4B). Based on the absorption coefficients of both PSs, an average number of 807 Ce6 molecules and 202 RB molecules were conjugated with $M13_{FR\alpha}$. The higher loading of Ce6 compared with RB can be attributed to differences in conjugation chemistry, the solubility of the two PS derivatives, and the number of accessible reactive sites on pVIII.

Further confirmation of Ce6 and RB bioconjugation to the major coat protein pVIII was provided by intact protein MS analysis (Fig. 2C).[41,42] The MW of WT pVIII was observed at 5237 Da, which is consistent with the expected mass of the protein based on the amino acid sequence.[50] The pVIII + RB conjugate was observed at 6384 Da, corresponding to the addition of RB-PEG$_3$-ONH$_2$ (1165 Da) and the loss of a water molecule. Similarly, pVIII + Ce6 conjugate was observed at 5816 Da, due to the amidic coupling with Ce6-NHS (693 Da) and the loss of NHS leaving group.[48] Mass spectrometry characterizations demonstrated the effective bioconjugation of Ce6 and RB to pVIII protein, and we support the use of this technique for evaluating the effectiveness of chemical- or genetic-based modification of the major coat protein of M13 and other bacteriophages.

Light-induced ROS generation of $M13_{FR\alpha}$–Ce6–RB

Although the photophysical characteristics of Rose Bengal and chlorin e6 are well known as single molecules, their bioconjugation with carrier systems is frequently associated with a perturbation of their photodynamic performance. The main factor driving this behavior is related to their surrounding environment, characterized by a different polarity with respect to the aqueous solution, as well as the presence of chemical functionalities, affecting the redox properties of the excited states.

In general, PSs absorb light at a specific wavelength, transitioning from the ground state to the first singlet excited state (^{1}PS). Through intersystem crossing, the excitation can be further transferred to the triplet excited state (^{3}PS), characterized by a relatively long lifetime. Molecular oxygen could interact with ^{3}PS *via* two main pathways: (i) the type I mechanism, involving electron transfer and leading to the formation of various reactive oxygen species and hydrogen peroxide as stable species; (ii) the type II mechanism, based on energy transfer, resulting in the production of singlet oxygen. We evaluated the photodynamic ability of the $M13_{FR\alpha}$–Ce6–RB bioconjugate subjected to green and red light irradiation, comparing the performance of each unconjugated PS with the

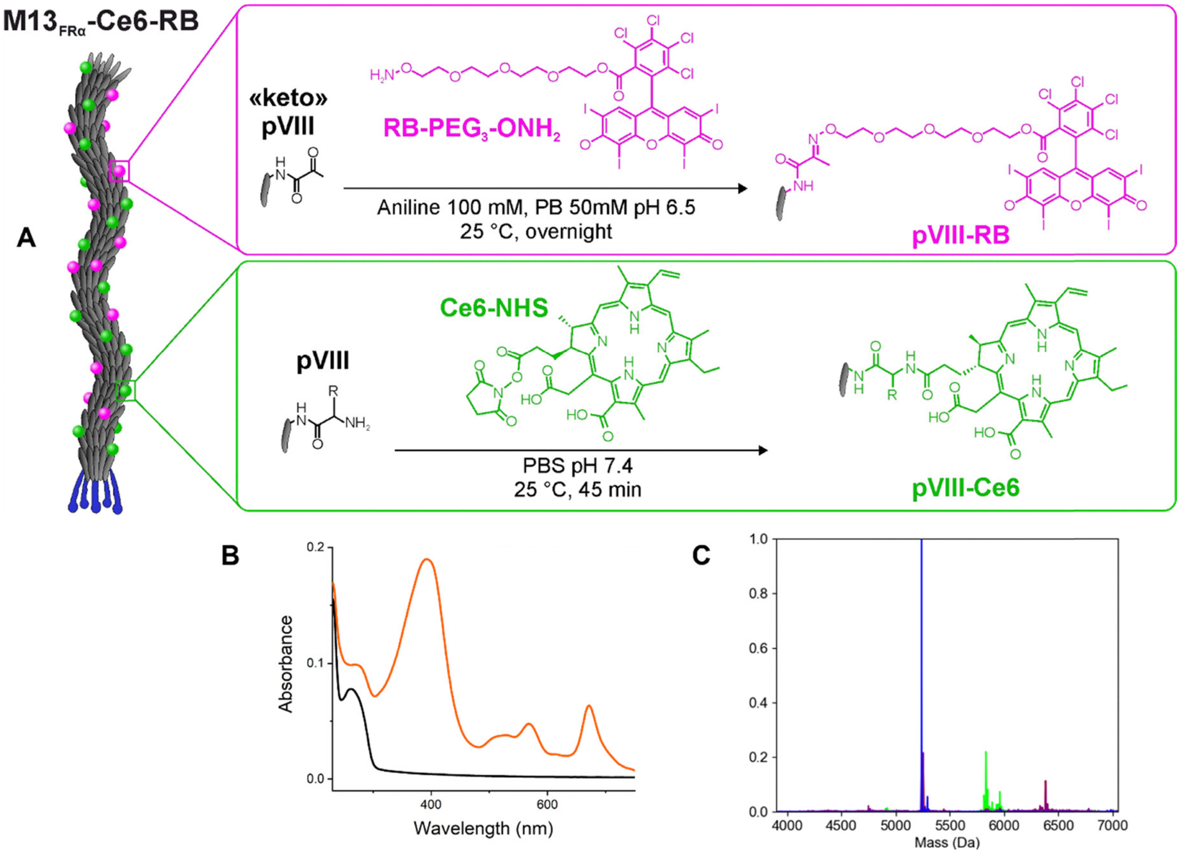

Fig. 2 (A) Schematic representation of the multimodal bioconjugation techniques of RB-PEG$_3$-ONH$_2$ (purple frame) and Ce6-NHS (green frame) performed onto the M13$_{FR\alpha}$ major capsid protein (pVIII). (B) UV-Vis spectra of M13$_{FR\alpha}$–Ce6–RB (orange line) and M13$_{FR\alpha}$ (black line). (C) Deconvolved MS spectra of unconjugated pVIII protein (blue line), conjugated pVIII-RB protein (purple line) and conjugated pVIII-Ce6 protein (green line). Mass spectra deconvolution performed with Unidec Software.[49]

bioconjugate. Moreover, the role of the irradiation sources was evaluated, irradiating the sample with (i) a green LED, mostly suitable for RB excitation, (ii) a red LED, specific for Ce6 excitation, and (iii) their combination, activating both PSs.

The Amplex Red assay was used to monitor the ROS production following the type I mechanism, while the type II mechanism was monitored by using the ABMDMA assay. Fig. 3A demonstrates a dose-dependent production of H_2O_2 by the M13$_{FR\alpha}$–Ce6–RB in the sub-micromolar range of PS concentration. The contribution to peroxide generation from an equal amount of free Ce6 and RB molecules is reported separately, suggesting a dominant contribution of the Ce6 to the type I mechanism, as expected (Fig. 3A). As previously reported in similar studies,[36] the ABMDMA assay (Fig. S6A) demonstrated a higher generation of $^1O_2$ from free Ce6 compared to M13$_{FR\alpha}$–Ce6–RB. The same experiment was carried out, comparing the amount of ROS produced by irradiating the bioconjugate with red and green LEDs, both separately and in combination (Fig. 3B and Fig. S6B). Under all these irradiating setup conditions, the results always demonstrate a dose-dependent increase in ROS production, showing similar performance for red and green light; however, a significant enhancement of both peroxide production and singlet oxygen for combined irradiation can be observed. Collectively, light-induced ROS production assessment demonstrates that multiple wavelength irradiation and dual functionalization enhance the ability of M13$_{FR\alpha}$ bioconjugate to generate peroxides. The switch from type II to type I mechanism after their conjugation is a phenomenon already observed for Ce6 and RB in our previous studies.[36,51] The electron-rich environment provided by the capsid proteins facilitates the electron-transfer mechanism, without further addition of an external electron-donating group. Due to the lower dependence on oxygen concentration, the enhancement of the type I mechanism plays in favor of the treatment, allowing PDT also in tumor tissues characterized by a hypoxic environment.[52,53]

Targeting, uptake, and imaging assessment of M13$_{FR\alpha}$–Ce6–RB bioconjugates *in vitro*

One of the main limitations of using immunoconjugates is their decrease, or even loss, of selectivity after bioconjugation of therapeutic molecules, as well as aggregation phenomena that hinder their exploitation. UV-Vis spectra (Fig. 2B) demonstrate the good stability of M13$_{FR\alpha}$–Ce6–RB in physiological conditions. Therefore, we assessed its targeting properties using the two cell lines previously selected, *i.e.*, OV90 and OC314, which display high and low FRα expression, respectively. Taking advantage of their fluorescent properties, we exploited Ce6 and

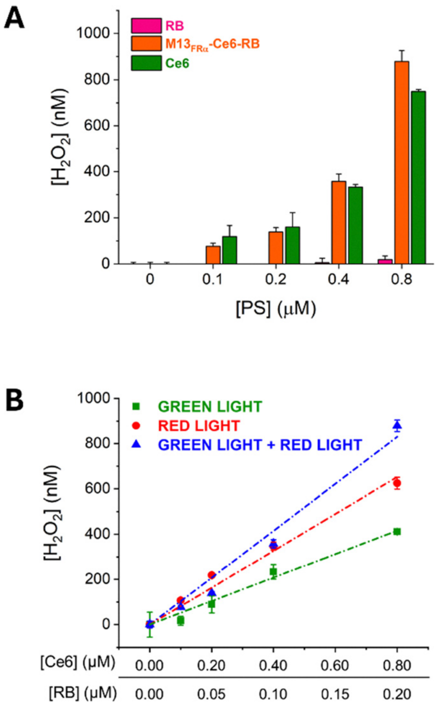

Fig. 3 (A) Generation of peroxides using different concentrations of Ce6 (green bar), RB (magenta bar), and M13$_{FR\alpha}$–Ce6–RB (orange bar) upon combined green and red light irradiation. (B) Overall peroxides production trend of the M13$_{FR\alpha}$–Ce6–RB bioconjugate upon the three different irradiation modalities: green light (green), red light (red), and combined green and red lights (blue).

RB as imaging agents as well, allowing the monitoring of the phage internalization and intracellular localization without using further imaging probes. Confocal microscopy experiments and semi-quantitative analysis demonstrate that the bioconjugates also retain their specificity toward FRα. The results clearly demonstrated that Ce6–RB conjugated M13$_{FR\alpha}$ are internalized within both cancer cell lines (Fig. 4A, B and D, E), with significantly higher uptake from OV90, in accordance with the results obtained with the unconjugated vector (shown in Fig. 1K). Due to the higher loading, the intensity of the fluorescence signal mainly comes from Ce6; however, a significant correlation between RB and Ce6 fluorescence was observed on both cell lines, with a Pearson's *R* value of 0.81 and 0.82 on OV90 and OC314, respectively (Fig. 4C and F). This observation confirmed the stability of the refactored phage supramolecular assembly, also after covalent conjugation. To further confirm the cellular uptake and demonstrate the flexibility of the platform as a phototheranostic agent, flow cytometry analysis was conducted on both cell lines, testing Ce6–RB conjugates. Monitoring the fluorescence signals of Ce6 and RB, reported in the *x* and *y* axes, respectively, allows a clear interpretation of the data (Fig. 4G, H and J, K). The shift of the peak of Ce6 fluorescence toward higher intensity, compared to the untreated control, can be observed for both cell lines treated with M13$_{FR\alpha}$–Ce6–RB, displaying an increase in fluorescence in both Ce6 and RB channels. Despite the low expression of FRα, a significant internalization of the conjugates is clearly observed in the OC314 cell line (Fig. 4L). In any condition, the mean fluorescence intensity (MFI) increase is higher for the cell line overexpressing FRα (*i.e.*, OV90, Fig. 4I), confirming the retargeting ability of the conjugates and the consequent receptor-mediated internalization of the PSs. These results are in perfect agreement with the fluorescent microscopy studies, suggesting that a stable targeted phototheranostic platform has been synthesized. Due to the flexibility of chemical conjugation, standard fluorescence-based assessments can be employed to detect cancer cells overexpressing specific receptors. This approach enables real-time monitoring of internalization and subcellular localization, resulting in a useful tool for diagnosis and fluorescence-guided surgery.

Photodynamic eradication of OV90 and OC314 ovarian cancer cell lines

The previous results clearly demonstrated the M13$_{FR\alpha}$–Ce6–RB capability to (i) generate ROS under irradiating conditions, (ii) selectively target, and (iii) penetrate FRα-positive OC cells, meeting key criteria required by an ideal 3rd generation PS. To evaluate its PDT performance on OV90 and OC314 cell lines, we exposed cells to increasing concentrations of M13$_{FR\alpha}$–Ce6–RB within the sub-micromolar PS range, corresponding to picomolar concentrations of the phage carrier. After incubation and washing, cells were irradiated with the same LED sources used for ROS assessment, either separately or in combination, and subsequently subjected to viability analysis. Cells treated with M13$_{FR\alpha}$–Ce6–RB and maintained in the dark showed no statistically significant reduction in viability across the tested PS concentration range, up to 0.8 μM Ce6-equivalent concentration (Fig. 5A), confirming the safety profile of the conjugates under these conditions. By contrast, light exposure induced a concentration-dependent decrease in viability. Separate red and green irradiation produced comparable IC$_{50}$ values for both for OV90 (green IC$_{50}$ 64 nM, red IC$_{50}$ 54 nM) and OC314 (green IC$_{50}$ 141 nM, red IC$_{50}$ 120 nM), with a slightly better performance under red light irradiation (Fig. 5B and C). Notably, combining the two light sources further enhanced PDT efficacy, resulting in a substantial IC$_{50}$ decrease in OC314 (78 nM) and a modest improvement in OV90 (51 nM) (Fig. 5D). To better dissect the contribution of each photosensitizer, additional PDT experiments were performed using the single-PS conjugates M13$_{FR\alpha}$–Ce6 and M13$_{FR\alpha}$–RB, as well as the corresponding free photosensitizers, under red, green, and combined irradiation conditions (Fig. S9). As expected, Ce6-containing systems showed preferential activity under red light, whereas RB-containing systems were more efficiently activated under green light. Under combined irradiation, the dual construct displayed the broadest photoresponse and the highest overall photocytotoxicity. By contrast, the corresponding free photosensitizers at equivalent concentrations showed negligible cytotoxicity, highlighting that the engineered phage is a central functional component of the platform, as it enables targeted delivery and high local photosensitizer density, thereby markedly enhancing PDT efficacy. Collectively, these findings illustrate how irradiation conditions and the multifunctional design

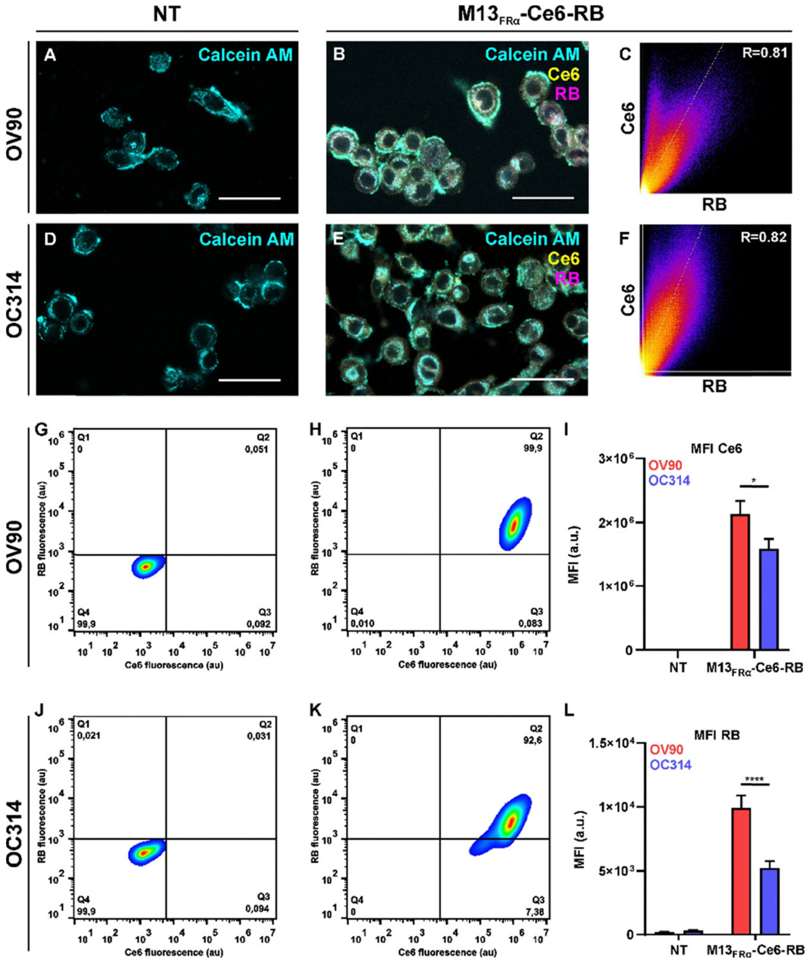

Fig. 4 Enhanced targeting of the $M13_{FR\alpha}$–Ce6–RB towards OC cells, significantly higher for OV90 cells. Confocal microscopy analysis of the $M13_{FR\alpha}$ bioconjugates tropism on OV90 (A)–(C) and OC314 (D)–(F) incubated with PBS (A) and (D) and $M13_{FR\alpha}$–Ce6–RB (B) and (E). The cytoplasmic compartment was stained with Calcein AM (cyan), Ce6 is in yellow, while RB is in magenta. Scale bar = 50 μm. (C) and (F) Colocalization analysis between RB and Ce6 signal performed on (B) and (E). White line is the tendency line, and *R* shows Pearson's *R* value calculated with Fiji Coloc2. Flow cytometry analyses were performed with the same concentration of $M13_{FR\alpha}$–Ce6–RB on OV90 (G)–(I) and OC314 (J)–(L) incubated with PBS (G) and (J) and $M13_{FR\alpha}$–Ce6–RB (H) and (K). (I) and (L) Are mean fluorescence intensity (MFI) measured in flow cytometry in RB and Ce6 channels, respectively. All graphs and calculations were performed using Graphpad Prism and FlowJo™. Statistical significance was calculated by one-way parametric ANOVA followed by Dunnet's multiple comparison test * $p < 0.05$; ** $p < 0.01$; **** $p < 0.0001$; $n = 3$.

of $M13_{FR\alpha}$ influence therapeutic response in distinct ovarian cancer cell lines. By leveraging fundamental photophysical and bioconjugation principles, the therapeutic performance of the photosensitizing agent can be further optimized. Importantly, the combined light source increases the PDT potency of M13–Ce6–RB in the low-FRα-expressing OC314 line, highlighting that dual-light activation can improve efficacy even at lower photosensitizer concentrations.

Multiwavelength irradiation of platinum-resistant OV90 and OC314 cell lines treated with $M13_{FR\alpha}$–Ce6–RB

PDT has been proposed as an adjuvant treatment that, in combination with chemotherapy, aims at preventing the onset of chemoresistance.[15,16,54,55] Among the different chemotherapeutics used, cisplatin was the first platinum-based agent approved for the treatment of several tumors, including OC.[55–57] The efficacy of platinum derivatives currently used in the clinics, such as carboplatin, is limited by the onset of resistance.[58–60] Consequently, there is a pressing need to develop new therapeutic strategies and to evaluate their ability to eradicate platinum-resistant tumors. To explore the translational potential of our platform to address this cogent clinical issue, we assess the PDT performances of $M13_{FR\alpha}$–Ce6–RB in the platinum-resistant OV90 and OC314 cell lines using the optimized irradiation setup that maximizes photokilling. Despite chemoresistance to platinum-derivatives, both cell lines retained strong sensitivity to PDT, yielding IC_{50} values of 50 nM and 61 nM for OV90 and OC314, respectively (Fig. 5F), which essentially overlap with those observed in the corresponding sensitive lines. This indicates that platinum resistance does not diminish the PDT efficacy of $M13_{FR\alpha}$–Ce6–RB. Consistent with previous observations, no reduction in cell viability was detected under dark conditions, confirming the favorable safety profile of the conjugates (Fig. 5E).

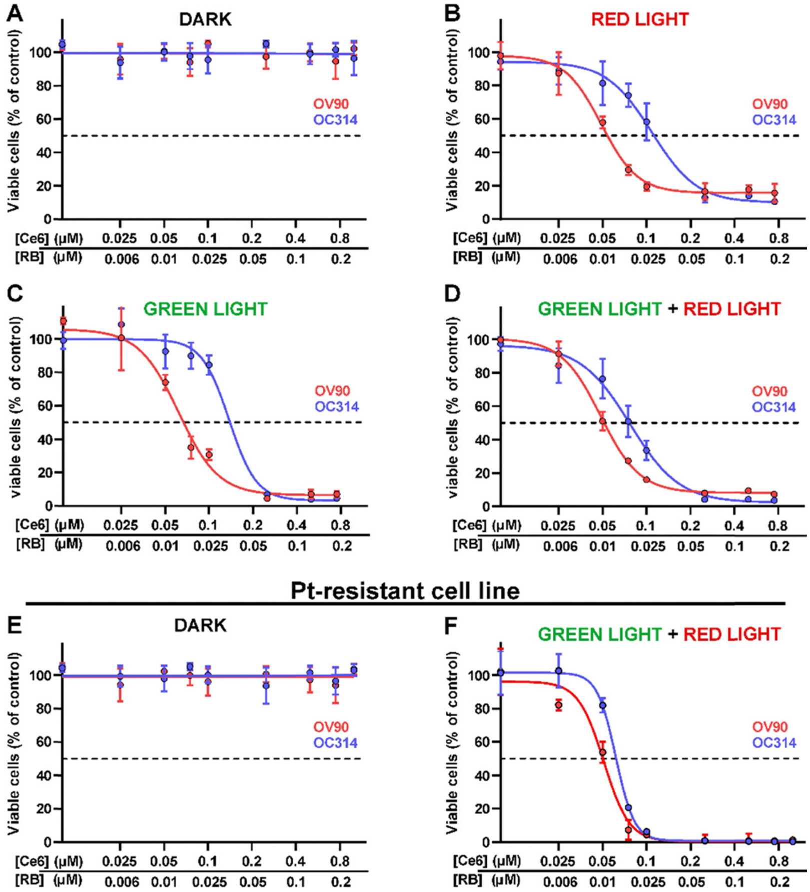

Fig. 5 Photoirradiated M13$_{\mathrm{FR}\alpha}$–Ce6–RB strongly decreases OC cell viability. Cytotoxic effects of M13$_{\mathrm{FR}\alpha}$–Ce6–RB on OV90 and OC314 cells kept in the dark (DARK, (A), and (E)) or irradiated with a RED (B) or GREEN (C) LED light or with both (D) and (F), 24 h after treatment. Cell viability was analyzed using the MTT test on three independent biological replicates (n = 3). IC$_{50}$ values were calculated by parametric nonlinear regression absolute IC$_{50}$ using GraphPadPRISM.

Conclusions

The genetically engineered M13$_{\mathrm{FR}\alpha}$ phage marks a step forward for the design of a modular targeted nanoplatform. By combining precise genetic retargeting with orthogonal chemical conjugation, the present work demonstrates for the first time the construction of a phototheranostic biotechnological scaffold simultaneously displaying a tumor-selective ligand and multiple photosensitizers with complementary photophysical profiles. A key feature of this platform is the *de novo* engineering of a MORAb-003–derived scFv and its genetic display on M13, providing high-affinity targeting of FRα-positive ovarian cancer cells while maintaining the structural integrity of the engineered phage. The resulting M13$_{\mathrm{FR}\alpha}$–Ce6–RB construct successfully integrates tumor targeting, imaging capability, and light-triggered cytotoxicity within a single biocompatible platform.

The selective binding of M13$_{\mathrm{FR}\alpha}$ to folate receptor alpha-overexpressing ovarian cancer cells, together with the enhanced photodynamic response under dual-wavelength irradiation, highlights the efficiency of this hybrid biological-chemical approach. Notably, platinum-resistant ovarian cancer cell lines retained strong sensitivity to PDT, confirming that chemoresistance to platinum compounds does not compromise the therapeutic performance of the conjugate. This finding supports the potential of M13$_{\mathrm{FR}\alpha}$–Ce6–RB as an adjuvant or standalone intervention in settings where conventional chemotherapy fails.

We also report the first native ESI-MS analysis of the pIII minor coat proteins, enabling straightforward identification of the genetically expressed targeting moieties displayed on M13 phage, as well as both the wild-type and chemically modified pVIII major coat proteins. This approach provides an additional analytical tool for characterizing engineered phage platforms and complements existing methodologies. The current investigation is based on 2D *in vitro* models, which are well suited to assess targeting specificity, cellular uptake, and photocytotoxicity. These results provide a strong basis for further validation in more complex biological settings, where tissue architecture, diffusion barriers, and tumor heterogeneity can be more faithfully captured.

Overall, these results open novel avenues for the design of multifunctional platforms, based on M13$_{\mathrm{FR}\alpha}$-bioconjugates, for imaging-guided photodynamic therapy, including as an adjuvant strategy for targeting OC cells, including those displaying features of acquired chemoresistance. Furthermore, considering that FRα is also found at high levels in breast cancer (35–70%), lung cancer (15–75%), and endometrial cancer (20–50%), $M13_{FR\alpha}$-bioconjugates could be easily adapted for theranostic applications on other malignancies.[61,62]

Experimental

Materials

Rose Bengal (Cat. No. 330000), pyridoxal 5′-phosphate monohydrate (PLP) (Cat. No. 82870), poly(ethylene glycol) PEG BioUltra, 8000 (Cat. No. 89510-F), *N*-hydroxysuccinimide (NHS) (Cat. No. 130672), *N*-(3-dimethylaminopropyl)-*N*′-ethylcarbodiimide hydrochloride (EDC) (Cat. No. 03450), sodium bicarbonate (Cat. No. 31437-M), sodium carbonate (Cat. No. 223530), 9,10-anthracenediylbis(methylene)dimalonic acid (ABMDMA) (Cat. No. 75068), 10-acetyl-3,7-dihydroxyphenoxazine (Amplex Red) (Cat. No. 90101), type VI-A peroxidase from horseradish lyophilized powder (HRP) (Cat. No. P6782), hydrogen peroxide solution 30% (w/w) (Cat. No. 31642-M), sodium chloride (Cat. No. S9888-M), potassium phosphate monobasic (Cat. No. P0662-M), sodium phosphate dibasic (Cat. No. S0876), potassium chloride (Cat. No. P3911M), Amicon Ultra centrifugal filters (MWCO 30 kDa, Millipore UFC503024, Cat. No. Z677892-24EA), dimethyl sulfoxide (DMSO) (Cat. No. 472301), deuterium oxide (Cat. No. 151882) and other solvents were purchased from Sigma Aldrich (Merck, Darmstadt, Germany). Aminooxy-PEG_3-bromide HCl salt (Cat. No. BP-23143) was purchased from BroadPharm (6625 Top Gun Street, Suite 103 San Diego, CA 92121). Chlorin e6 (Item No. 21684) was purchased from Cayman Chemical (Ann Arbour, MI, USA). All reagents were used without further purification. Milli-Q water was used for the preparation of all aqueous solutions.

Cell cultures

The OV90, human epithelial ovarian carcinoma; the OC314, ovarian cancer; the CAOV3, human epithelial ovarian adenocarcinoma, and the SKOV3, human ovarian adenocarcinoma, cell lines were propagated in DMEM medium supplemented with 10% heat-inactivated fetal bovine serum (FBS), 1% penicillin–streptomycin solution 100 U mL^{-1} and 1% L-glutamine 200 mM (Euroclone, Italy). While the OVSAHO, high-grade serous ovarian carcinoma, cell line was propagated in RPMI-1640 medium supplemented with 10% heat-inactivated fetal bovine serum (FBS), 1% penicillin–streptomycin solution 100 U mL^{-1} and 1% L-glutamine 200 mM (Euroclone, Italy). Cells were grown at 37 °C in a humidified incubator with 5% CO_2. Validation of cell lines was obtained *via* Sanger sequencing of p53 driver mutation[63] (Table S1). Cells were grown at 37 °C in a humidified incubator with 5% CO_2. Platinum-resistant cell models were generated from chemosensitive OC314 and OV90 cell lines as previously described, referred to as OC314cis[63] and OV90cis.[64] Both models were cultured in the same condition as their corresponding parental lines and, to preserve chemoresistance to both cis- and carboplatin, every six passages in culture they were treated with CDDP at their respective IC_{50}.

Design, production, and purification of $M13_{FR\alpha}$ phage

Cloning. The single-chain variable fragment sequence of MORAb-003 (farletuzumab),[23] specific for folate receptor α, was designed by fusing the variable regions of the heavy and light chains with a flexible $(GGGGS)_3$ linker. The resulting scFv construct was codon-optimized for *E. coli* expression and synthesized commercially (OfficinaeBio, Italy) into a pSEVA plasmid backbone. For phagemid construction, the expression backbone pPK3003A was used. pPK3003A was designed based on the pComb3XSS plasmid backbone with the substitution of the pLAC promoter with the rhamnose-inducible promoter pRham. The pPK3003A was linearized by PCR using primer pairs GGATCCCCATCTGGTGGTTC and GGCCGATGCGCTAAACGC, and the scFv insert was amplified using primers tagcgtttagcgcatcggccGAAGTACAACTGGTTGAATC and gaaccaccagatggggatccTTTGATTTCAACTTTGGTGC to generate complementary overhangs for so-called AQUA cloning.[65] Following transformation into chemically competent *E. coli* DH5α, positive clones were verified by colony PCR, and successful insertion was confirmed *via* Sanger sequencing (Eurofins Genomics, Germany).

Phage production and purification. Recombinant $M13_{FR\alpha}$ phages were produced in *E. coli* DH5α cells co-transformed with the hyperphage helper plasmid M13K07Δf1oriΔpIII and the previously cloned pK3003A-MORAb phagemid. Co-transformants growth on LB agar plates supplemented with ampicillin (100 μg mL^{-1}) and kanamycin (25 μg mL^{-1}) were inoculated in 400 mL LB medium supplemented with antibiotics (ampicillin and kanamycin) and rhamnose (5 mM) to induce expression of modified pIII. Cultures were grown at 30 °C for 24 h with agitation, and phages were purified through PEG/NaCl and isoelectric point precipitations.[66] Briefly, cells were pelleted by centrifugation (12 000*g*, 25 min, 4 °C), and the phage-containing supernatant was incubated with PEG 8000 (4% w/v) and NaCl (3% w/v) for 1 h on ice, and centrifuged at 10 000*g* for 30 min at 4 °C. The resulting pellet was resuspended in PBS (pH 7.4), and the suspension pH was adjusted to 4.2 with 0.5 M HCl to reach the M13 isoelectric point, followed by centrifugation (12 000*g*, 25 min, 4 °C). The purified phage pellet was resuspended in PBS, centrifuged at 6000*g* for 10 minutes, to remove possible bacteria, and the supernatant was transferred to a new tube.

In vitro quantification of FRα expression and $M13_{FR\alpha}$ tropism

Confocal microscopy. For immunofluorescence analysis, 3 × 10^4 cells were seeded onto round glass coverslips (12 mm, VWR) placed in 6-well plates (Corning, USA) in complete medium and incubated overnight at 37 °C under 5% CO_2. The following day, coverslips were gently washed with PBS and fixed with 4% paraformaldehyde (PFA) for 15 min at room temperature (RT). Cells were then washed twice with PBS containing 0.05% Tween-20 (wash buffer, permeabilized using 0.1% Triton X-100 in PBS for 10 min and subsequently blocked in 2% skim milk (w/v) in wash buffer for 45 min at RT under gentle agitation. Cells were incubated for 1 h with anti-FRα monoclonal antibody (1 : 500, Invitrogen, MA5-23917, clone 548908) diluted in 2% skim milk (w/v) in wash buffer, washed twice with wash buffer, and stained for 1 h with Alexa Fluor® 488-conjugated goat anti-mouse secondary antibody (1 : 1000, Invitrogen). Nuclei were counterstained with Hoechst 33342 (1 μg mL^{-1}, 15 min), and coverslips were mounted in PBS.

For visualization of receptor-specific phage binding, 3 × 10^4 cells were seeded on a glass coverslip and incubated overnight at 37 °C. Cells were treated with 500 μL complete medium containing 1 × 10^{12} M13$_{\text{FR}\alpha}$ phages. After 45 min incubation at 37 °C, cells were washed twice with PBS, fixed with 4% PFA for 15 min, permeabilized with 0.1% Triton X-100 for 10 min, and blocked with 2% milk in wash buffer for 45 min. Phages were detected using anti-pVIII monoclonal antibody (ProGen, 1 : 500) for 1 h, followed by Alexa Fluor® 488-conjugated secondary antibody (1 : 1000) for 1 h. Nuclei were stained with Hoechst 33342 for 15 min, and coverslips were mounted in PBS. Imaging was performed on a Nikon A1R confocal microscope under identical acquisition settings for all conditions.

For studying the tropism of bioconjugated M13$_{\text{FR}\alpha}$, cells were seeded, incubated with phages and washed as already described. Next, live OC cells were stained for 15 min with Hoechst 33342, and the fluorescence of Ce6 and RB was monitored on a Nikon A1R confocal microscope. RB fluorescence was acquired using the 561 nm laser line and 595/50 nm detection channel, whereas Ce6 fluorescence was acquired using the 402 nm laser line and 700/75 nm detection channel. Signals were acquired sequentially to minimize channel crosstalk. Under these acquisition conditions, spectral crosstalk between the two channels is negligible.

Flow cytometry. For quantitative assessment of FRα expression, 1 × 10^6 cells were harvested, resuspended in 1 mL complete medium, and centrifuged at 900 × *g* for 5 min. Cells were fixed using 4% PFA for 15 min at RT, washed with wash buffer, and blocked in 2% milk (w/v) in wash buffer for 45 min. Cells were incubated with anti-FRα antibody (1 : 500, Invitrogen, MA5-23917, clone 548908) for 1 h, washed twice with wash buffer, and subsequently incubated with Alexa Fluor® 488-conjugated goat anti-mouse IgG (1 : 1000, Invitrogen) for 1 h at RT. After two final wash buffer washes, cells were resuspended in PBS for acquisition.

Similarly, for quantitative evaluation of tropism, 1 × 10^6 cells were incubated with 1 × 10^{12} M13$_{\text{FR}\alpha}$ phages in complete medium for 45 min at 37 °C. After washing twice with wash buffer, cells were fixed with 4% PFA for 15 min and blocked with 2% milk for 45 min. Samples were stained with anti-pVIII antibody (1 : 500, ProGen) for 1 h, followed by Alexa Fluor® 488-secondary antibody (1 : 1000) for 1 h.

Tropism of conjugated phages was performed on live cells as follows. Cells (3 × 10^5 per well) were seeded in 6-well plates and incubated overnight at 37 °C. The next day, cells were exposed to M13$_{\text{FR}\alpha}$–Ce6–RB (4 μM Ce6 and 1 μM RB final concentration) in 500 μL of complete medium for 45 min at 37 °C. After incubation, cells were washed twice with PBS, detached with 1× trypsin for 5 min at 37 °C, and resuspended in medium. Following centrifugation at 900*g* for 5 min, pellets were resuspended in 300 μL PBS for analysis. NT controls (no phage incubation) were included.

For the competition assay, 3 × 10^5 OV90 cells were incubated with anti-FRα monoclonal antibody (1 : 100, Invitrogen, MA5-11205) for 1 h or with PBS (untreated) at 37 °C. Subsequently, 1 × 10^{11} M13FRα were added to the cells, and the mixture was incubated for a further 45 minutes at 37 °C. The OV90 cells were then washed twice with PBS, trypsinised, fixed with 4% paraformaldehyde for 15 minutes at room temperature (RT), and subsequently blocked in 2% skimmed milk powder (w/v) in PBS-Tween for 45 minutes at RT under gentle agitation. The cells were then incubated for 1 h with anti-pVIII-FITC monoclonal antibody (1 : 500, PROGEN, 61497), diluted in 2% skimmed milk in PBS-Tween. Finally, cells were washed twice with PBS-Tween, resuspended in PBS and acquisition was performed on a Beckman Coulter CytoFLEX S flow cytometer.

Flow cytometric analyses were performed on a Beckman Coulter CytoFLEX S flow cytometer. Cell populations were gated on forward and side scatter parameters. Alexa Fluor 488 emission was detected in the FITC channel (excitation 488 nm, emission 525/40 nm). Additional fluorophores were recorded as follows: RB in PE (561 nm → 585/42 nm), Ce6 in Violet660 (405 nm → 660/610 nm). Median fluorescence fold-increase over controls was used to quantify receptor expression or phage binding. At least 10 000 events per sample were recorded. Data were analyzed using CytExpert (Beckman Coulter) and FlowJo (BD Biosciences).

Bioconjugation and purification of M13$_{\text{FR}\alpha}$–Ce6

Synthesis of Ce6 succinimidyl ester (Ce6-NHS). In a two-neck round-bottom flask under nitrogen atmosphere, chlorin e6 (15.61 mg, 0.026 mmol, 1.0 eq.) is dissolved with 1 mL anhydrous DMF under stirring conditions. Then, *N*-hydroxy succinimide (4.52 mg, 0.039 mmol, 1.5 eq.) and EDC (5.1 mg, 0.026 mmol, 1.0 eq.) are added to the reaction mixture. The reaction is kept under continuous stirring, in dark conditions at room temperature overnight. The crude mixture is then evaporated under reduced pressure to remove DMF. The green solid obtained is dissolved in DCM and extracted first with 100 mM PBS (2 × 10 mL) and then with H_2O (2 × 10 mL). The product obtained is used with no further purification. Yield after work-up 60%.

UV-Vis (DMSO): $\lambda_{\max}$ 408 nm; 666 nm (Fig. S4A).

ESI-MS (MeOH): 693.20 $[M]^+$; 666.20 $[M–CHCH_2]^+$; 664.15 $[M–CH_2CH_3]^+$; 596.14 $[M–NHS/Ce6]^+$; 551.00 $[M–NHS–CO_2]^+$ (Fig. S7).

Synthesis of M13$_{\text{FR}\alpha}$–Ce6

To a M13$_{\text{FR}\alpha}$ solution (40 nM; 2.4 × 10^{13} virions per mL) in PBS is added an appropriate volume of a stock solution of Ce6-NHS (20 mM in DMSO) to reach a final dye concentration of 0.5 mM (3.5 eq. with respect to the available pVIII amines in the reaction mixture). The mixture is incubated under stirring conditions (700 rpm) at 25 °C for 45 minutes. Bioconjugates are then purified *via* size exclusion chromatography (SEC) desalting columns (PD-10, G25 Sephadex® resin) to remove unbound dye.

Bioconjugation and purification of M13$_{FR\alpha}$–Ce6–RB

Synthesis of Rose Bengal alkoxyamine-derivative (RB-PEG$_3$-ONH$_2$). In a two-neck round-bottom flask under nitrogen atmosphere, Rose Bengal disodium salt (33.54 mg, 0.03 mmol, 1.5 eq.) is dissolved in 2 mL anhydrous DMF under stirring conditions. Then, Br-PEG$_3$-ONH$_2$ (6.78 mg, 0.02 mmol, 1 eq.) is solubilized in 2 mL of anhydrous DMF dropwise and the solution is added to the RB solution. The reaction is kept under continuous stirring at 80 °C overnight.[67] After reaction completion (evaluated by TLC), DMF is removed under reduced pressure. The purple solid is solubilized in ethyl acetate and extracted with H_2O (2 × 10 mL), subsequently with $NaHCO_3$ 5% aq. (2 × 10 mL) and finally with Brine. The extracted product is used with no further purification. Yield after workup 50%. UV-Vis (DMSO): λ_{max} 565 nm (Fig. S4B). ^1H NMR spectrum was recorded on a Bruker Ascend 600 MHz with a 5 mm probe; chemical shifts (δ) are reported in ppm and coupling constants in Hertz (Hz).

^1H NMR (600 MHz, DMSO-d_6) δ 7.41 (s, 2H), 4.13–4.06 (m, 1H), 4.02 (m, 1H), 3.71 (td, J = 5.2, 4.6, 1.2 Hz, 1H), 3.66 (td, J = 5.2, 4.6, 1.2 Hz 1H), 3.62–3.47 (m, 12H) (Fig. S8).

Site-selective bioconjugation of RB-ONH$_2$ to M13$_{FR\alpha}$ and M13$_{FR\alpha}$–Ce6 and purification of the bioconjugates

Step 1 – PLP transamination. To an M13$_{FR\alpha}$ (final concentration in the reaction mixture 40 nM; 2.4 × 10^{13} virions per mL) solution in PB 50 mM (pH 6.5) is added an appropriate volume of a PLP stock solution (50 mM in PB 50 mM pH 6.5) to reach a final concentration of 6.8 mM of PLP (100 eq. with respect to the pVIII N-terminal amines). Reaction is incubated at 25 °C, 700 rpm overnight. The reaction mixture is then purified to remove PLP through three cycles of PEG 4%/NaCl 3% precipitation. Equivolume of a 2× solution of PEG/NaCl is added to the sample, then it is put into an ice bath for one hour. The sample is centrifuged (14 000*g*, 4 °C, 20 min), and the resulting pellet is resuspended in PB 50 mM.

Step 2 – RB-PEG$_3$-ONH$_2$ bioconjugation (oxime formation). Transaminated M13$_{FR\alpha}$ phages from Step 1 are resuspended in PB 50 mM (pH 6.5) to obtain a final concentration of 40 nM (2.4 × 10^{13} virions per mL). Subsequently, an appropriate volume of a stock solution of RB-PEG$_3$-ONH$_2$ (50 mM in DMSO) is added to reach a final concentration of 140 μM (2 eq. with respect to the N-terminal pVIII amines). Finally, aniline is added to reach a concentration of 100 mM. The reaction mixture is kept under magnetic stirring conditions at room temperature overnight. Bioconjugates are purified using SEC desalting columns to remove unbound dye.

Characterization of M13$_{FR\alpha}$ bioconjugates

UV-vis spectroscopic characterization of M13$_{FR\alpha}$-bioconjugates. For the spectroscopic characterization of M13$_{FR\alpha}$-bioconjugates, absorption spectra were recorded using a Cary60 UV-Vis spectrophotometer (Agilent). Following the Smith formula, the absorption band centred at 269 nm is used for the quantification of M13$_{FR\alpha}$ for the synthesis (Fig. 2B).

Mass spectrometry

The phage samples were analyzed by LC-MS analysis of the denaturated capsid proteins. In detail, 160 μL of phage sample was processed to separate capsid proteins from nucleic acids and impurities according to Wessel *et al.*[41] Briefly, the proteins were precipitated by consecutive addition of a volume ratio of 4 : 1 : 3; methanol : chloroform : water, with extensive vortexing between each addition. Under these conditions, a protein pellet could be easily isolated between the lipophilic (chloroform) and hydrophilic (methanol and water) phases. Both liquid phases were discarded, and the pellet was further washed with methanol, dried under N2 and stored at −20 °C. For UPLC-HRMS analysis, 10 μl of formic acid 80% was added and the samples were stored at −20 °C for 2 min. Then, the samples were pipetted 5 times and stored for an additional 8 min at −20 °C. Eventually, the samples were diluted with 390 μl of HPLC-grade water at 4 °C. After centrifugation at 10 000 rpm for 5 min, the top 350 μl were collected for protein determination. The chromatographic separation was achieved with an ACQUITY UPLC H-Class PLUS (Waters) equipped with an ACQUITY UPLC 2.1 × 150 mm protein BEH C4 column (300 Å pore size, 1.7 μm particle size) operating at 65 °C. The solvent A was HPLC-grade water at 0.1% formic acid, and solvent B was acetonitrile at 0.1% formic acid. The analysis was performed at 0.4 mL min^{-1} flow as follows with regard to solvent B: 0–1 min step at 10%, 1–18 min gradient reaching 50%, 18–20 min step at 50%, 20–21 min gradient reaching 90%, 21–23 min step at 90%, 23–24 min gradient reaching 10%, 24–26 min step at 10%. Protein detection was achieved with an Xevo G2-XS quadrupole time-of-flight (QToF) mass spectrometer with the following settings: capillary voltage 2.5 kV; sample cone: 60 V; source T: 150 °C; desolvation T: 600 °C; cone gas: 50 L h^{-1}; desolvation gas: 900 L h^{-1}. Chromatographic analysis and MS spectra deconvolution were performed on raw data using Unidec software 5.0.2 version (University of Oxford, Oxford, UK).

Photodynamic performances of bioconjugated M13$_{FR\alpha}$

Irradiating conditions. All irradiation experiments were performed under standardized conditions to ensure reproducibility across all assays. Samples were irradiated using a V-TAC 50 W VT-4752 RGB SMD floodlight, providing green and red emission profiles (Fig. S5). Irradiance was measured directly at the sample surface using a Delta Ohm LP 471 RAD photoradiometer, and the corresponding light dose was calculated based on an irradiation time of 15 minutes. Under these conditions, the red and green LEDs delivered an irradiance of 6.7 and 7.1 mW cm^{-2}, corresponding to a light dose of 6.0 and 6.4 J cm^{-2}, respectively. For combined irradiation, the sum of the green and red light doses was delivered. The distance between the light source and the samples was kept constant at 19 cm. These conditions were consistently applied for ROS generation assays (ABMDMA and Amplex Red) and for cell viability experiments.

Quantification of ROS generation

ABMDMA assay. To detect and quantify singlet oxygen ($^1O_2$) production of Ce6, Rose Bengal, and M13$_{\mathrm{FR}\alpha}$–Ce6–RB upon irradiation, the ABMDMA assay was performed. ABMDMA reacts selectively with singlet oxygen, and the reaction progress can be monitored by measuring the decrease in the UV absorption bands of ABMDMA. Solutions of Ce6 and RB were prepared in deuterated PBS, whereas for the M13$_{\mathrm{FR}\alpha}$-bioconjugate, PBS was exchanged with deuterated PBS. A volume of 97 μL from each sample (0.8 μM, 0.4 μM, 0.2 μM and 0.1 μM of photosensitizer calculated through UV-vis absorption spectra) and 3 μL of 5 mM ABMDMA in DMSO were dispensed into 96-well plates designated for light irradiation. Absorbance before and after irradiation was recorded at 401 nm using an EnSpire® Multimode Plate Reader (PerkinElmer, Waltham, MA, USA).

Amplex Red assay. The Amplex Red assay was employed to quantify the peroxides produced by the irradiated samples. This method relies on an enzymatic reaction catalyzed by horseradish peroxidase (HRP), in which the non-fluorescent Amplex Red reacts with peroxides to form fluorescent resorufin.[39]

For each sample, 90 μL were pipetted into three different 96-well plates. Two plates were irradiated under the same conditions used for the ABMDMA assay, while one was kept in the dark. A working solution (WS) containing Amplex Red and HRP dissolved in 50 mM phosphate buffer was freshly prepared, and 10 μL of WS were added to each well. The plates were then incubated for 30 minutes in the dark at room temperature.

The fluorescence emission of resorufin was measured at 590 nm (λ_{ex} 560 nm) using an EnSpire® Multimode Plate Reader (PerkinElmer). The fluorescence values were converted into H_2O_2 concentrations using a calibration curve obtained from standard H_2O_2 solutions. The concentration of H_2O_2 generated by the irradiated samples was calculated by subtracting the amount produced by the corresponding dark controls.

Cell viability assay. About 20 000 cells per well were seeded in 96-well flat-bottom plates (Corning) and incubated overnight. Afterwards, cells were treated for 45 minutes with complete medium supplemented with M13$_{\mathrm{FR}\alpha}$–Ce6–RB at different concentrations. Additional control experiments were performed under the same conditions using the single-PS conjugates M13$_{\mathrm{FR}\alpha}$–Ce6 and M13$_{\mathrm{FR}\alpha}$–RB, as well as the corresponding free photosensitizers (Ce6 and RB), at equivalent photosensitizer concentrations. Cells were washed twice with PBS and then irradiated in PBS for 15 minutes with a red and/or green LED source. At the end of the irradiation, PBS was removed, and cells were incubated in complete medium for 24 h at 37 °C with 5% CO_2.

Cell viability after PDT was evaluated by MTT assay. Briefly, the culture medium was replaced with fresh medium containing MTT (0.5 mg mL^{-1}), and cells were incubated for 90 min at 37 °C in a humidified 5% CO_2 atmosphere. The MTT-containing medium was then removed, and formazan crystals were solubilized in DMSO. Absorbance was measured at 570 nm (reference 690 nm) using an EnSpire multimode plate reader (PerkinElmer, USA). Data are presented as mean ± SD from at least three independent experiments.

Author contributions

Conceptualization: MDG, PC, AP; data curation: AK, AM, AC, MN, AP; formal analysis: PC, MDS, MDG; funding acquisition: MDG; investigation: AK, AM, MN, CDD, SC, MDL; methodology: AD, MC, GG, MDG, PC; project administration: MDG; resources: GG, MC, AD; supervision: MDG, PC; validation: MDS, AC, PC; visualization: all authors; writing – original draft: MDG, PC; writing – review & editing: all authors.

Conflicts of interest

There are no conflicts to declare.

Data availability

The data supporting this article have been included as part of the supplementary information (SI). Supplementary information: ScFv MORAB-003:VH-(GGGGS)$_3$-VL, pIII-Linker, pIII C-terminal domain sequence. Fig. S1. Western blot analysis performed on M13$_{\mathrm{FR}\alpha}$; Table S1. Validation of cell lines; Fig. S2 Flow cytometry peak profiles relative to Fig. 1; Fig. S3 Competition assay of M13$_{\mathrm{FR}}$M13$_{\mathrm{FR}\alpha\alpha}$ and anti-FRα mAb for FRα of OV90 cell line; Fig. S4. UV-Vis Spectra of RB-PEG$_3$-ONH$_2$ and Ce6-NHS; Fig. S5. Emission spectra of the green and red LED sources; Fig. S6. Singlet oxygen ABMDMA assay; Fig. S7. ESI-MS spectrum of Ce6-NHS; Fig. S8. ^{1}H NMR spectrum of RB-PEG$_3$-ONH$_2$; Fig. S9. *In vitro* PDT assessment of free Ce6 and RB and their corresponding conjugates with M13$_{\mathrm{FR}\alpha}$ under green, red and combined irradiation. See DOI: https://doi.org/10.1039/d5tb02844b.

Acknowledgements

The research leading to these results was funded by the Fondazione del Monte di Bologna e Ravenna (grant number 2023.0475). PhageLight project – P. I. Di Giosia Matteo. The research leading to these results was partly funded by Associazione Italiana Ricerca sul Cancro (AIRC) under IG 2019 – ID. 22921 project – P. I. Gasparre G. We gratefully acknowledge Associazione Orchestra per la Vita ONLUS for their donation, which contributed to acquiring the irradiation system used to optimize our experiments.

Notes and references

1 SEER, Ovarian Cancer—Cancer Stat Facts, https://seer.cancer.gov/statfacts/html/ovary.html, (accessed 31 October 2025).
2 U. A. Matulonis, A. K. Sood, L. Fallowfield, B. E. Howitt, J. Sehouli and B. Y. Karlan, *Nat. Rev. Dis. Primers*, 2016, **2**, 1–22.
3 S. Lheureux, M. Braunstein and A. M. Oza, *Ca-Cancer J. Clin.*, 2019, **69**, 280–304.
4 E. Kipps, D. S. P. Tan and S. B. Kaye, *Nat. Rev. Cancer*, 2013, **13**(4), 273–282.

5 S. Lheureux, C. Gourley, I. Vergote and A. M. Oza, *Lancet*, 2019, **393**, 1240–1253.

6 L. A. Torre, B. Trabert, C. E. DeSantis, K. D. Miller, G. Samimi, C. D. Runowicz, M. M. Gaudet, A. Jemal and R. L. Siegel, *Ca-Cancer J. Clin.*, 2018, **68**, 284–296.

7 G. Di Lorenzo, G. Ricci, G. M. Severini, F. Romano and S. Biffi, *Theranostics*, 2018, **8**, 4279–4294.

8 J. L. Tanyi, L. M. Randall, S. K. Chambers, K. A. Butler, I. S. Winer, C. L. Langstraat, E. S. Han, A. L. Vahrmeijer, H. S. Chon, M. A. Morgan, M. A. Powell, J. H. Tseng, A. S. Lopez and R. M. Wenham, *J. Clin. Oncol.*, 2023, **41**, 276–284.

9 D. E. J. G. J. Dolmans, D. Fukumura and R. K. Jain, *Nat. Rev. Cancer*, 2003, **3**, 380–387.

10 L. Ulfo, P. E. Costantini, M. Di Giosia, A. Danielli and M. Calvaresi, *Pharmaceutics*, 2022, **14**, 241.

11 G. Gunaydin, M. E. Gedik and S. Ayan, *Front. Chem.*, 2021, **9**, 686303.

12 A. P. Castano, P. Mroz and M. R. Hamblin, *Nat. Rev. Cancer*, 2006, **6**, 535–545.

13 E. Teplinsky and F. Muggia, *Transl. Cancer Res.*, 2015, **4**, 107–117.

14 T. Michy, T. Massias, C. Bernard, L. Vanwonterghem, M. Henry, M. Guidetti, G. Royal, J. L. Coll, I. Texier, V. Josserand and A. Hurbin, *Cancers*, 2019, **11**(11), 1760.

15 R. Liu, Y. Gao, N. Liu and Y. Suo, *Photodiagn. Photodyn. Ther.*, 2021, **33**, 102156.

16 A. I. Bilyalov, N. A. Shanazarov and S. V. Zinchenko, *Bionanoscience*, 2020, **10**, 807–810.

17 M. Lan, S. Zhao, W. Liu, C. Lee, W. Zhang and P. Wang, *Adv. Healthcare Mater.*, 2019, **8**, 1900132.

18 D. Gao, X. Guo, X. Zhang, S. Chen, Y. Wang, T. Chen, G. Huang, Y. Gao, Z. Tian and Z. Yang, *Mater. Today Bio*, 2020, **5**, 100035.

19 A. Cantelli, M. Malferrari, A. Soldà, G. Simonetti, S. Forni, E. Toscanella, E. J. Mattioli, F. Zerbetto, A. Zanelli, M. Di Giosia, M. Zangoli, G. Barbarella, S. Rapino, F. Di Maria and M. Calvaresi, *JACS Au*, 2021, **1**, 925–935.

20 K. R. Kalli, A. L. Oberg, G. L. Keeney, T. J. H. Christianson, P. S. Low, K. L. Knutson and L. C. Hartmann, *Gynecol. Oncol.*, 2008, **108**(3), 619–626.

21 M. Scaranti, E. Cojocaru, S. Banerjee and U. Banerji, *Nat. Rev. Clin. Oncol.*, 2020, **17**(6), 349–359.

22 S. Lheureux, M. Braunstein and A. M. Oza, *Ca-Cancer J. Clin.*, 2019, **69**, 280–304.

23 W. Ebel, E. L. Routhier, B. Foley, S. Jacob, J. M. McDonough, R. K. Patel, H. A. Turchin, Q. Chao, J. B. Kline, L. J. Old, M. D. Phillips, N. C. Nicolaides, P. M. Sass and L. Grasso, *Cancer Immun.*, 2007, **7**(1), 6.

24 J. Silverstein, A. Smick, B. Johnson and G. E. Konecny, *Future Oncol.*, 2025, **21**, 2143–2153.

25 I. Vergote, D. Armstrong, G. Scambia, M. Teneriello, J. Sehouli, C. Schweizer, S. C. Weil, A. Bamias, K. Fujiwara, K. Ochiai, C. Poole, V. Gorbunova, W. Wang, D. O'Shannessy and T. J. Herzog, *J. Clin. Oncol.*, 2016, **34**, 2271–2278.

26 T. Van Gorp, K. N. Moore, G. E. Konecny, A. Leary, Y. García-García, S. Banerjee, D. Lorusso, J. Y. Lee, J. W. Moroney, G. Caruso, D. Klasa-Mazurkiewicz, J. Tromp, L. P. Martin, S. Breuer, C. A. Leath, D. Cibula, S. J. Weroha, P. Estévez-García, D. M. O'Malley, R. E. Miller, L. Coffman, G. Scandurra, D. Berton, L. Li, E. Zagadailov, E. J. Diver, O. Trédan and F. Hilpert, *Lancet Oncol.*, 2025, **26**, 503–515.

27 G. P. C. Salmond and P. C. Fineran, *Nat. Rev. Microbiol.*, 2015, **13**(12), 777–786.

28 W. J. Chung, D. Y. Lee and S. Y. Yoo, *Int. J. Nanomed.*, 2014, **9**, 5825–5836.

29 K. A. Henry, M. Arbabi-Ghahroudi and J. K. Scott, *Front. Microbiol.*, 2015, **6**, 135114.

30 H. J. Stacey, S. De Soir and J. D. Jones, *Antibiotics*, 2022, **11**, 1340.

31 P. Jault, T. Leclerc, S. Jennes, J. P. Pirnay, Y. A. Que, G. Resch, A. F. Rousseau, F. Ravat, H. Carsin, R. Le Floch, J. V. Schaal, C. Soler, C. Fevre, I. Arnaud, L. Bretaudeau and J. Gabard, *Lancet Infect. Dis.*, 2019, **19**, 35–45.

32 R. M. Dedrick, C. A. Guerrero-Bustamante, R. A. Garlena, D. A. Russell, K. Ford, K. Harris, K. C. Gilmour, J. Soothill, D. Jacobs-Sera, R. T. Schooley, G. F. Hatfull and H. Spencer, *Nat. Med.*, 2019, **25**(5), 730–733.

33 D. Ghosh, A. G. Kohli, F. Moser, D. Endy and A. M. Belcher, *ACS Synth. Biol.*, 2012, **1**, 576–582.

34 V. A. Petrenko and P. K. Jayanna, *FEBS Lett.*, 2014, **588**, 341–349.

35 S. K. Zadran, N. Facchinello, P. De Rosa, R. Saporetti, P. E. Costantini, L. Ulfo, M. Nigro, A. Petrosino, L. Pappagallo, S. Aloisi, G. Milazzo, Z. A. Din, A. Rigamonti, L. Flora, M. Santulli, L. Cimadom, G. Zuccheri, M. Zangoli, M. Di Sante, M. Di Giosia, F. Di Maria, R. Bernardoni, E. Barbieri, M. Calvaresi, A. Danielli and G. Perini, *Adv. Sci.*, 2025, **12**, e15356.

36 B. Bortot, M. Apollonio, G. Baj, L. Andolfi, L. Zupin, S. Crovella, M. di Giosia, A. Cantelli, R. Saporetti, L. Ulfo, A. Petrosino, G. Di Lorenzo, F. Romano, G. Ricci, M. Mongiat, A. Danielli, M. Calvaresi and S. Biffi, *Free Radical Biol. Med.*, 2022, **179**, 242–251.

37 L. Ulfo, A. Cantelli, A. Petrosino, P. E. Costantini, M. Nigro, F. Starinieri, E. Turrini, S. K. Zadran, G. Zuccheri, R. Saporetti, M. Di Giosia, A. Danielli and M. Calvaresi, *Nanoscale*, 2022, **14**, 632–641.

38 E. Turrini, L. Ulfo, P. E. Costantini, R. Saporetti, M. Di Giosia, M. Nigro, A. Petrosino, L. Pappagallo, A. Kaltenbrunner, A. Cantelli, V. Pellicioni, E. Catanzaro, C. Fimognari, M. Calvaresi and A. Danielli, *Cell. Mol. Life Sci.*, 2024, **81**, 144.

39 P. E. Costantini, R. Saporetti, M. Iencharelli, S. Flammini, M. Montrone, G. Sanità, V. De Felice, E. J. Mattioli, M. Zangoli, L. Ulfo, M. Nigro, T. Rossi, M. Di Giosia, E. Esposito, F. Di Maria, A. Tino, C. Tortiglione, A. Danielli and M. Calvaresi, *Small*, 2025, **21**, 2405832.

40 A. Petrosino, R. Saporetti, F. Starinieri, E. Sarti, L. Ulfo, L. Boselli, A. Cantelli, A. Morini, S. K. Zadran, G. Zuccheri, Z. Pasquini, M. Di Giosia, L. Prodi, P. P. Pompa,

P. E. Costantini, M. Calvaresi and A. Danielli, *iScience*, 2023, **26**, 108032.

41 D. Wessel and U. I. Flügge, *Anal. Biochem.*, 1984, **138**, 141–143.

42 D. P. Donnelly, C. M. Rawlins, C. J. DeHart, L. Fornelli, L. F. Schachner, Z. Lin, J. L. Lippens, K. C. Aluri, R. Sarin, B. Chen, C. Lantz, W. Jung, K. R. Johnson, A. Koller, J. J. Wolff, I. D. G. Campuzano, J. R. Auclair, A. R. Ivanov, J. P. Whitelegge, L. Paša-Tolić, J. Chamot-Rooke, P. O. Danis, L. M. Smith, Y. O. Tsybin, J. A. Loo, Y. Ge, N. L. Kelleher and J. N. Agar, *Nat. Methods*, 2019, **16**(7), 587–594.

43 G. T. Hess, J. J. Cragnolini, M. W. Popp, M. A. Allen, S. K. Dougan, E. Spooner, H. L. Ploegh, A. M. Belcher and C. P. Guimaraes, *Bioconjugate Chem.*, 2012, **23**, 1478–1487.

44 L. Berglund, E. Björling, P. Oksvold, L. Fagerberg, A. Asplund, C. A. K. Szigyarto, A. Persson, J. Ottosson, H. Wernérus, P. Nilsson, E. Lundberg, Å. Sivertsson, S. Navani, K. Wester, C. Kampf, S. Hobert, F. Pontén and M. Uhlén, *Mol. Cell. Proteomics*, 2008, **7**, 2019–2027.

45 H. Jin, C. Zhang, M. Zwahlen, K. von Feilitzen, M. Karlsson, M. Shi, M. Yuan, X. Song, X. Li, H. Yang, H. Turkez, L. Fagerberg, M. Uhlén and A. Mardinoglu, *Nat. Commun.*, 2023, **14**(1), 5417.

46 The Human Protein Atlas, https://www.proteinatlas.org/, (accessed 17 December 2025).

47 S. L. Hulin-Curtis, J. A. Davies, D. Nestić, E. A. Bates, A. T. Baker, T. G. Cunliffe, D. Majhen, J. D. Chester and A. L. Parker, *Cancer Gene Ther.*, 2020, **27**(10), 785–798.

48 L. Xing, Y. Xu, K. Sun, H. Wang, F. Zhang, Z. Zhou, J. Zhang, F. Zhang, B. Caliskan, Z. Qiu and M. Wang, *Sci. Rep.*, 2018, **8**(1), 1–13.

49 M. T. Marty, A. J. Baldwin, E. G. Marklund, G. K. A. Hochberg, J. L. P. Benesch and C. V. Robinson, *Anal. Chem.*, 2015, **87**, 4370–4376.

50 O. Morag, N. G. Sgourakis, D. Baker and A. Goldbourt, *Proc. Natl. Acad. Sci. U. S. A.*, 2015, **112**, 971–976.

51 A. Cantelli, F. Piro, P. Pecchini, M. Di Giosia, A. Danielli and M. Calvaresi, *J. Photochem. Photobiol., B*, 2020, **206**, 111852.

52 L. Shi, F. Hu, Y. Duan, W. Wu, J. Dong, X. Meng, X. Zhu and B. Liu, *ACS Nano*, 2020, **14**, 2183–2190.

53 K. Chen, P. He, Z. Wang and B. Z. Tang, *ACS Nano*, 2021, **15**, 7735–7743.

54 T. Michy, T. Massias, C. Bernard, L. Vanwonterghem, M. Henry, M. Guidetti, G. Royal, J.-L. Coll, I. Texier, V. Josserand, A. Hurbin, T. Michy, T. Massias, C. Bernard, L. Vanwonterghem, M. Henry, M. Guidetti, G. Royal, J.-L. Coll, I. Texier, V. Josserand and A. Hurbin, *Cancers*, 2019, **11**(11), 1760.

55 C. Arnau del Valle, P. Srivastava, K. McNaughton and H. C. Huang, *Bioeng. Transl. Med.*, 2025, e70031.

56 S. Ghosh, *Bioorg. Chem.*, 2019, **88**, 102925.

57 N. Spears, F. Lopes, A. Stefansdottir, V. Rossi, M. De Felici, R. A. Anderson and F. G. Klinger, *Hum. Reprod. Update*, 2019, **25**, 673–693.

58 M. Song, M. Cui and K. Liu, *Eur. J. Med. Chem.*, 2022, **232**, 114205.

59 L. Amable, *Pharmacol. Res.*, 2016, **106**, 27–36.

60 R. M. McQuade, V. Stojanovska, J. C. Bornstein and K. Nurgali, *Pharmacol. Res.*, 2018, **137**, 104–113.

61 G. F. Zannoni, A. Santoro, A. d'Amati, N. D'Alessandris, G. Scaglione, B. Padial Urtueta, M. Valente, N. Narducci, F. Addante, S. Spadola, E. Bragantini and G. Angelico, *Int. J. Mol. Sci.*, 2025, **26**, 5222.

62 M. Scaranti, E. Cojocaru, S. Banerjee and U. Banerji, *Nat. Rev. Clin. Oncol.*, 2020, **17**(6), 349–359.

63 S. Miglietta, M. Sollazzo, I. Gherardi, S. Milioni, B. Cavina, L. Marchio, M. De Luise, C. A. Coada, M. Fiorillo, A. M. Perrone, I. Kurelac, G. Gasparre, L. Iommarini, A. M. Ghelli and A. M. Porcelli, *Open Biol.*, 2025, **15**(1), 240151.

64 M. De Luise, I. Kurelac, S. Coluccelli, A. De Leo, E. M. Bartoszek, M. Iorio, M. Grillini, C. A. Coadă, D. de Biase, L. Marchio, M. N. López, N. Rimmer, A. M. Perrone, P. De Iaco, A. M. Porcelli, V. Heinzelmann, I. Martin, F. Jacob, M. G. Muraro and G. Gasparre, *npj Precis. Oncol.*, 2025, **9**(1), 152.

65 H. M. Beyer, P. Gonschorek, S. L. Samodelov, M. Meier, W. Weber and M. D. Zurbriggen, *PLoS One*, 2015, **10**, e0137652.

66 P. Passaretti, I. Khan, T. R. Dafforn and P. Goldberg Oppenheimer, *Sci. Rep.*, 2020, **10**(1), 1–9.

67 N. Sugita, K. I. Kawabata, K. Sasaki, I. Sakata and S. I. Umemura, *Bioconjugate Chem.*, 2007, **18**, 866–873.